

GT2019-90931

FLOW IN A SCALED TURBINE COOLANT CHANNEL WITH ROUGHNESS DUE TO ADDITIVE MANUFACTURING

David R. Hanson
The Pennsylvania State University
State College, PA, USA

Stephen T. McClain
Baylor University
Waco, TX, USA

Jacob C. Snyder
The Pennsylvania State University
State College, PA, USA

Robert F. Kunz
The Pennsylvania State University
State College, PA, USA

Karen A. Thole
The Pennsylvania State University
State College, PA, USA

ABSTRACT

Additive manufacturing (AM) approaches such as Laser Powder Bed Fusion (L-PBF) are being explored to reduce manufacturing costs of gas turbine components. Surfaces of additively manufactured components exhibit distinctive roughness characteristics that significantly affect the pressure losses and heat transfer. For this study, a coupon with a vertical internal flow passage was created using L-PBF and characterized using x-ray tomography. The roughness pattern was extracted using the spanwise-planar extraction approach. Also, two surfaces consisting of distributions of ellipsoids were created to capture the important statistical characteristics of the original rough surface. The resulting roughness geometries were scaled by 102x and applied to the internal wall of the Roughness Internal Flow Tunnel (RIFT). Measurements of friction losses and velocity profiles were obtained. Detailed Reynolds-Averaged Navier Stokes (RANS) simulations using grid-resolved roughness of flow in the RIFT were also performed using an in-house Computational Fluid Dynamics (CFD) code. The present approach combining experimental measurements and CFD simulation of an up-scaled roughness coupon provides a more detailed picture of the flow-field within the roughened channel than was previously available. The measured friction factor of the baseline up-scaled rough channel is within 15% of the original engine-scale channel within the fully turbulent regime. The ellipsoid surfaces are seen to have a friction factor 30% lower than the up-scaled rough channel; the authors hypothesize that this is due to bulk span-wise ridges being present in the up-scaled rough surface but not in the ellipsoid surfaces.

INTRODUCTION

Additive manufacturing (AM) approaches are being explored as an approach to creating complex gas-turbine components such as cooling holes. Unlike subtractive manufacturing approaches, AM does not require linear material removal paths such as milling or electron-discharge machining. AM allows for the construction of components with complicated external shapes and internal structures. The ability to create complex internal structures suggests that internal cooling passages for gas turbines can be designed and optimized in ways not possible with cored-casting approaches.

AM offers significant design advantages but also presents unique challenges for engine-scale cooling channels. The most relevant AM approaches are laser powder bed fusion (L-PBF) approaches. The process creates surface roughness because of the layered-powder structure that differs depending on the material, build parameters, and orientation of the surface during the manufacturing process.

The roughness inherent to L-PBF cooling channels is especially important to the resulting pressure-loss and heat transfer because of its large size in relation to the channel dimensions. The equivalent sand-grain roughness height for an AM microchannel may be ten to fifty percent of the hydraulic diameter [1]. To enable engine designers to build AM turbine components with internal cooling passages, the nature of roughness created during L-PBF process must be better understood. Toward that end, the present paper details an effort to study experimentally and computationally the flow over roughness typical of an AM cooling channel. The uniqueness of this work consists in scaling up the channel roughness geometry 102x and studying the resulting flow in a wind-tunnel setting; this allows a higher Reynolds number regime and for the flow

itself to be studied in more detail than in previous works. Note that the scaled-up experiments have a much lower flow speed (bulk flow speed for all cases is less than 16 m/s; the engine-scale experiment has flow speed of approximately 100 m/s at the highest Reynolds number) than the engine-scale experiments for a given Reynolds number. Because of this difference, compressibility effects that may be present in the engine-scale experiments are not captured in the present scaled-up flows. No attempt is made to compensate for compressibility effects.

BACKGROUND

To understand the pressure loss and heat transfer behavior of AM cooling features, Stimpson *et al.* [1] performed a systematic experimental investigation of ten engine-scale rectangular-cross-section additively manufactured cooling microchannels fabricated from a powdered cobalt-chrome-molybdenum superalloy (CoCr) or Inconel 718. The authors found that imperfections of the additively manufactured channels were sufficiently large that uncertainty in the hydraulic diameter dominated the total uncertainty in the friction-factor measurements at fully-turbulent Reynolds numbers. Geometric imperfections were especially severe for surfaces that were downward-facing during fabrication. Arithmetic-averaged roughness heights (R_a) for these channels were between one and three percent of the hydraulic diameter. Consideration of the pressure-loss measurements showed that the most extreme case had an equivalent sand-grain roughness height of approximately $0.45 \times D_h$. Such roughness of comparable size to the channel caused poor agreement [2] with established sand-grain height correlations such as that of Flack and Schultz [3]. Stimpson *et al.* [1] proposed a new correlation for equivalent sand-grain roughness height based on the arithmetic roughness height.

Snyder *et al.* [4] investigated the effect of the build direction on the geometric imperfections and the resulting pressure-loss and heat transfer for a series of five channels with dimensions comparable to those of Stimpson *et al.* [1]. This study likewise found geometric imperfection to be the largest source of uncertainty in the pressure-loss measurements at high Reynolds numbers.

In a series of papers, Kirsch and Thole [5] [6] [7] explored the potential to use AM to fabricate non-traditional cooling hole geometries. Channels with stream-wise waves constructed of circular arcs [5] and channels with wave-geometry optimized numerically using the adjoint method [6] were fabricated. The channels had dimensions, build parameters, and surface roughness comparable to those studied by Stimpson *et al.* [1]. Heat transfer augmentation outperformed the straight AM microchannel, providing a design argument for using such non-traditional designs. Unfortunately, pressure-loss also increased substantially. Comparison of the pressure-loss measurements with smooth-walled numerical predictions of the channels performance [6] [7] showed a dramatic under-prediction of the friction factor.

In the efforts of Stimpson *et al.* [1] and Stimpson *et al.* [2], Snyder *et al.* [4], and Kirsch and Thole [5] [6] [7], detailed flow diagnostics could not be used to investigate the friction losses

and heat transfer in AM cooling channels because each study employed realistic blade-scale passages. These detailed flow diagnostics are crucial toward understanding how AM roughness impacts the flow. Further, detailed flow diagnostics are required for studying AM microchannels computationally, especially in the context of numerically optimizing the channel geometry.

APPROACH

The ultimate objective of the present work is to isolate the differences of AM roughness relative to traditional roughness by exploring the frictional interaction of AM roughness with internal flows. Toward that end, an engine-scale coupon with a vertical internal flow passage was created using L-PBF. The coupon internal passage roughness was characterized using x-ray tomography; the internal passage friction flow losses were characterized using the approach of References [1, 4, 5, 6, 7, 8].

A model of the AM surface following removal of bulk geometric imperfections was created; these imperfections are stream-wise and spanwise variations in the point cloud that are at length scales much larger than individual roughness elements. To achieve removal of the geometric imperfections and isolate the AM roughness, the two-dimensional, self-organizing-map with Z-axis regression (2D-SOM-ZR) approach of McClain [8] was employed.

The surface computational model was scaled for three-dimensional printing. The printed solid models were then used as the walls of an internal flow test rig for friction testing and hot-film anemometry diagnostics.

Analog (or surrogate) surfaces were created which replicate statistics and hydraulic characteristics of the original AM surface. Analog surfaces with deterministic roughness elements were developed based on the approach of Clemenson *et al.* [9]. The analog surfaces were constructed to match the equivalent sand-grain height predicted by the correlation of Flack and Schultz [3] for the scaled roughness coupon. This allowed isolation of fundamental differences in AM roughness from the traditional three-dimensional roughness employed in the roughness literature.

The bulk flow frictional losses and velocity profiles of each of the surfaces were investigated. The bulk flow loss behavior and velocity profiles allow comparison 1) to the classic Moody/Colebrook behavior described by the Moody diagram for classical roughness and 2) to the bulk flow losses measured in the engine-scale AM test article.

Finally, channel flow with the scaled AM roughness and the analog roughness patterns was investigated with steady Reynolds-Averaged Navier Stokes (RANS) Computational Fluid Dynamics (CFD) simulations employing grid-resolved roughness. The RANS simulations represent an attempt to validate standard computational approaches for predicting flow interactions with surfaces exhibiting AM roughness. Validations of these tools are needed to enable their use in designing additively-manufactured gas turbine components.

EXPERIMENTAL APPROACH

Two batteries of experimental measurements were acquired for this work. The first is a set of pressure-drop measurements taken in a small, engine-scale additively-manufactured channel. The second is pressure-drop and velocity profile measurements taken in the Roughness Internal Flow Tunnel (RIFT) on three 102x-scale roughness coupons intended to represent the small-scale channel roughness to varying degrees. For consistency with the notation of Stimpson et al [1], the small-scale channel will be referred to as “L-2x-Ha”. The up-scaled roughness coupons are referred to as the “Real_x102”, “Ellipsoid Analog”, and “Elliptical Cone Analog” surfaces.

L-2x-Ha Laser Powder Bed Fusion Flow Channels

Two engine-scale test coupons were manufactured for use in this study using a state-of-the-art L-PBF machine and Hastelloy-X (a nickel-chromium-iron-molybdenum alloy) powder [10]. The first was a flow coupon matching the nominal “L-2x-Co” and “L-2x-In” geometries used by Stimpson et al. [1] for measurements of bulk pressure loss and heat transfer. This flow coupon was built using the same orientation and support structures as described in the Stimpson study (channel axis at 45 degrees to the horizontal), but with different material and process parameters. The resulting channel has nominal dimensions 24.5 mm L x 2 mm H x 0.9 mm W (2.2:1 aspect ratio, $D_h \approx 1.24$ mm).

To allow detailed roughness characterization, a second, smaller coupon was built by extracting a section of the flow coupon design. This sacrificial roughness coupon was built in the same orientation and with the same parameters as the flow coupon, matching the thermo-mechanical conditions experienced by the parts during the build. Consequently, the channel surfaces of the roughness coupon could be analyzed and assumed to represent the surfaces present in the flow coupon with good confidence.

L-2x-Ha Roughness Surface Coupon Creation

High resolution x-ray Computed Tomography (CT) was used to generate a detailed 3D representation of the internal channel surface. X-ray CT characterization was chosen for its ability to resolve 3D features without requiring line of sight. Typically, a main limitation of using CT for surface analysis is the resolution. Both the size and material of the part being scanned can limit the achievable resolution to a value larger than the roughness features of interest. To overcome this limitation, the sacrificial roughness coupon was cut open to create a small sample containing a single wall of the internal channels. The upskin, or upward-facing surface, was chosen as the wall for analysis in this study. Because of the roughness sample’s small size, a scan could be completed at a resolution of 4 microns. The mean powder diameter was 35 microns for this build; scanning at 4 microns, therefore, allowed most of the partially melted particles on the surface to be resolved.

From the scan of the internal channel wall, the surface was determined to within 0.5 micron of its true location using an established software algorithm [11] used previously by Stimpson et al. [1] and Snyder et al. [4]. This surface was then sampled at

a 4 micron resolution to generate a point cloud for further processing. The resulting surface is shown in Figure 1(a).

Surface Analysis and Roughness Extraction

Spanwise and stream-wise variations on scales larger than the roughness elements are apparent in the CT surface depicted in Figure 1(a). To focus only on the nature of additively manufactured component roughness, the large-scale variations were removed using a two-dimensional self-organizing map approach with z-axis planar surface fitting (2D-SOM-ZR) developed by McClain et al. [8]. For the 2D-SOM-ZR, the stream-wise variations of the point cloud were captured using twelve codebook vectors. The average spacing of the codebook vectors, also referred to as neurons, was 0.41 mm. In many aspects, the 2D-SOM-ZR approach behaves similarly to a high-pass filter with wavelength cut-outs of 0.82-mm in the stream-wise direction and 1.5-mm in the spanwise direction. The roughness pattern following the 2D-SOM-ZR implementation is presented in Figure 1(b).

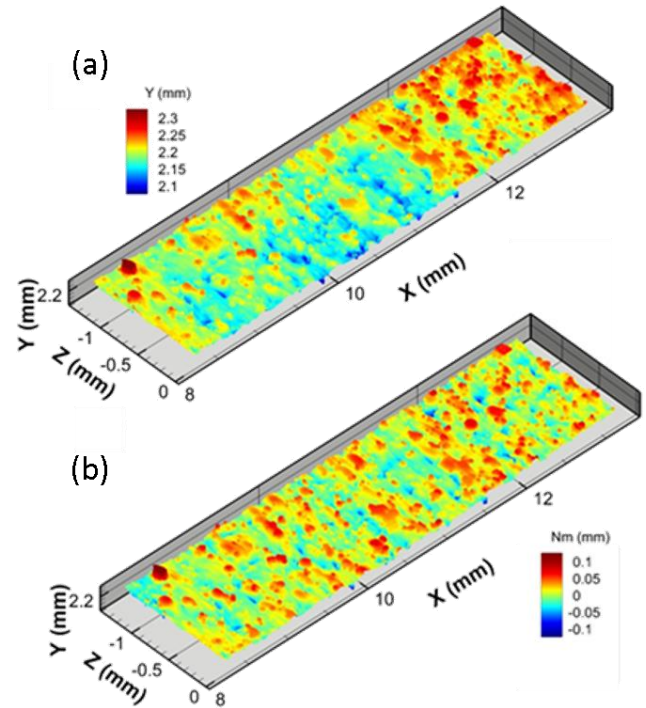


Figure 1 – CT scan results: (a) raw section with long wavelength spanwise and stream-wise variations and (b) long wavelength variations removed using 2D-SOM-ZR approach of McClain [8].

Analog Surface Generation

Clemenson et al. [9] presented an approach for developing analog or surrogate surface roughness patterns of deterministic roughness elements that replicates the skin friction and convection enhancement for a given real randomly rough surface. The approach is based on the following ideas. When representing a random surface roughness with consistent statistical properties in the stream-wise direction, 1) an analog

surface must be multi-spectral and 2) the primary shear and convective enhancements are caused by vortex shedding from the individual roughness elements and the interaction of the vortices with the next downstream roughness elements. The present method addresses the first idea by generating a random pattern of roughness elements that is then scaled to match chosen statistics of the surface. The second idea is addressed by matching the dominant wavelength in the stream-wise autocorrelation between the original and analog surfaces. Both of these points are discussed in detail in this section.

The approach of Clemenson *et al.* employs the two-dimensional autocorrelation function for the original rough surface using Eq. (1).

$$R_{AC}(\Delta x, \Delta z) = \left[\frac{1}{N_x N_z} \left| \sum Y'(x, z) \cdot Y'(x + \Delta x, z + \Delta z) \right| \right]^{\frac{1}{2}} \times \text{sign} \left(\sum Y'(x, z) \cdot Y'(x + \Delta x, z + \Delta z) \right) \quad (1)$$

This form of the autocorrelation function was chosen because it results in a non-rectified representation of the surface with an $R_{AC}(0,0)$ value that equals the root-mean-square roughness height, R_q , where

$$R_q = \left[\frac{1}{N_p} \sum_{i=1}^{N_p} (Y'^2) \right]^{\frac{1}{2}} = R_{AC}(0,0). \quad (2)$$

To perform the auto-correlation, the surface is resampled on a Cartesian stream-wise and spanwise grid with even spacing.

The random pattern generator developed by Tecson and McClain [12] was then used to construct analog surfaces to represent the original additively manufactured roughness. The random distribution of elements (random in element base dimension and random in centroid placement) was then scaled or mapped to match important aspects of the autocorrelation function of Eq. (1) based on a selected “deterministic shape” of each roughness element. For the present study, the deterministic shapes employed were 1) half-ellipsoids and 2) elliptical cones. Note that the unit cell roughness surfaces generated in this manner were smaller than the Real_x102 panel. The artificial roughness surfaces were mirrored in both directions in order to fill the same area as the Real_x102.

For the “Ellipsoid Analog” surface, the eccentricity, ϵ , of the ellipsoids was set based on the ratio of the microscales of the Real_x102 surface in the stream-wise and spanwise direction. The roughness element eccentricity is computed as the average over all roughness elements of the stream-wise major axis divided by the spanwise major axis. The microscales of the Real_x102 surface were determined using the osculating parabola approach in each direction based on the autocorrelation function of Eq. (1). The element distribution was then stretched in the stream-wise direction to match the primary stream-wise wavelength of the Real_x102 surface. The distribution was then stretched (or squeezed) in the spanwise direction while simultaneously increasing the stream-wise major axis until the surface R_q value was matched. Finally, the distribution was

again stretched or squeezed in the spanwise direction until the skewness, as defined in Eq. (3), of the Real_x102 surface was matched.

$$Skw = \frac{1}{R_q^3} \left[\frac{1}{N_p} \sum_{i=1}^{N_p} (Y'^3) \right]. \quad (3)$$

Because the R_q and Skw values were matched, the method provides a surface with an equivalent sand-grain roughness value according to the Flack and Schultz [3] correlation, as defined in Eq. (4), that agrees with the value from the Real_x102 surface within 2%.

$$k_{s,FS} = 4.43 R_q (1 + Skw)^{1.37}. \quad (4)$$

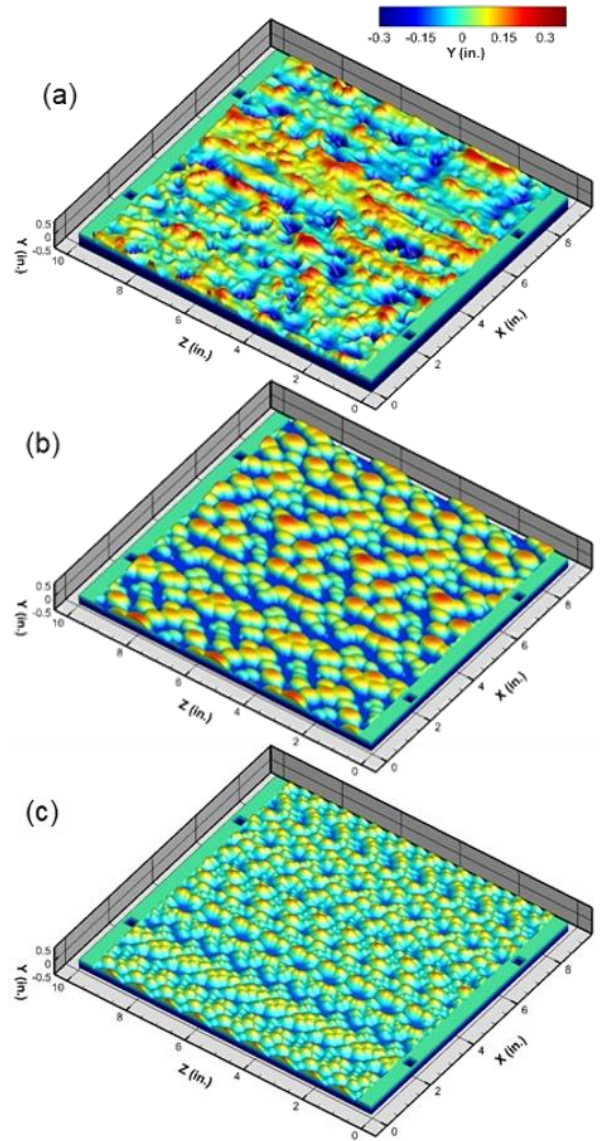


Figure 2 – Solid models of example roughness panels used in RIFT flow measurements: (a) Real_x102, (b) Ellipsoid Analog, and (c) Elliptical Cone Analog

The process of generating an analog surface is iterative because the statistical and autocorrelation analyses for the Ellipsoid Analog surface change as the distribution is stretched.

As was done for the Ellipsoid Analog surface, the eccentricity, ϵ , of the elliptical cones was set based on the ratio of the microscales of the Real_x102 surface. The primary stream-wise wavelength from the autocorrelation function was also matched. However, the negative skewness of the Real_x102 surface could not be matched with the ellipsoidal cone distribution. Consequently, the spanwise spacing of the distribution and diameter scales were set to minimize the skewness while matching the Flack and Schultz correlation for the equivalent sand-grain roughness parameter.

The stream-wise and spanwise autocorrelation functions for the Real_x102 and analog surfaces are shown in Figure 3. The stream-wise wavelength, marked as λ_x in Figure 3(a) and Table 1, is here defined as the distance from the origin to the first peak in the autocorrelation. Physically, this indicates the typical stream-wise distance from one roughness element to the next downstream. By constructing surfaces that match this stream-wise wavelength, the present method addresses the second idea given above: vortices that shed from roughness peaks and interact with downstream elements are the primary contributor to friction and convective enhancement.

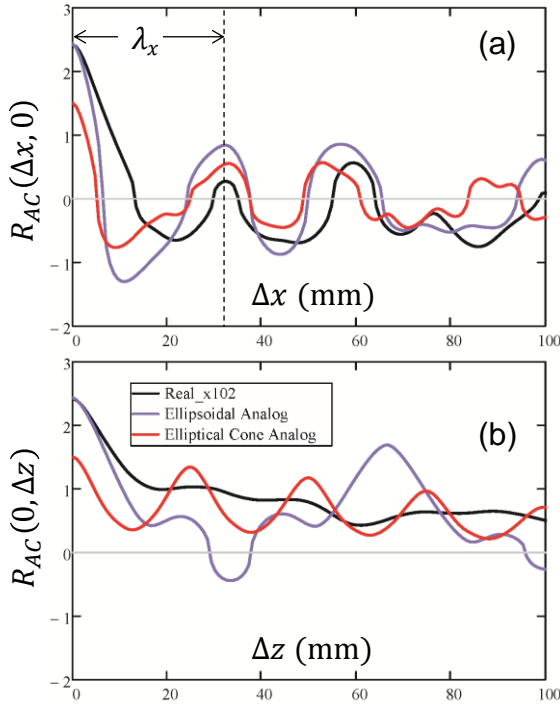


Figure 3 – Surface autocorrelation results for the surfaces investigated: (a) stream-wise results and (b) span-wise results

The resulting statistics for the Elliptical Cone Analog surface are presented in Table 1. The Ellipsoid Analog surface closely matches the stream-wise wavelength and statistical

properties of the Real_x102 surface. The Elliptical Cone Analog surface also matches the primary stream-wise wavelength. While the primary statistics of the Elliptical Cone Analog surface do not match the Real_x102 surface, the resulting prediction of equivalent sand-grain roughness from the Flack and Schultz correlation ($k_{s,F-S}$) agree within 2% of the Real_x102 surface.

While multiple spectral and statistical aspects of the Real_x102 surface are captured by each analog surface, two important aspects are not captured by the analog surfaces. The first parameter is the arithmetic mean roughness presented in Eq. (5).

$$R_a = \left[\frac{1}{N_p} \sum_{i=1}^{N_p} |Y'| \right] \quad (5)$$

As shown in Table 1, the R_a value for the Ellipsoid Analog surface is 10% higher than for the Real_x102 surface, while the R_a value for the Elliptical Cone Analog surface is 37% lower than the value for the Real_x102 surface. The difference in R_a values is important because other correlations besides the Flack and Schultz correlation for equivalent sand-grain roughness, such as that presented by Stimpson *et al.* [13], are based on R_a rather than R_q . The value of the equivalent sand-grain roughness predicted by Stimpson's correlation is called $k_{s,St}$ in Table 1. This correlation is a linear function of the arithmetic roughness height given by Eq. (6):

$$\frac{k_s}{D_h} = 18 \frac{R_a}{D_h} - 0.05, \quad (6)$$

for $R_a/D_h > 0.0028$.

Table 1 – Statistical and relative characteristics of the surfaces investigated

Metric	Real_x102	Ellipsoid Analog	Elliptical Cone Analog
R_a (mm)	1.887	2.075	1.214
R_q (mm)	2.436	2.419	1.504
$k_{s,F-S}$ (mm)	6.933	7.045	6.965
$k_{s,St}$ (mm)	30.85	34.24	18.73
λ_x (mm)	32.9	32.9	33.7
Skw	-0.276	-0.264	0.033
ϵ	0.693	0.693	0.693

The second aspect not captured by the analog surfaces is the span-wise autocorrelation of the Real_x102 surface. As shown in Figure 3(b), the spanwise autocorrelation for the Real_x102 surface does not cross $R_{AC} = 0$. This means that for additively manufactured surface roughness, when a large discrete roughness element occurs on the surface, it occurs on the top of a span-wise ridge in the surface profile. The span-wise ridges are suspected to be artifacts of the L-PBF process during which discrete layers of powder are deposited on the surface prior to controlled laser melting and binding of each layer to the previous

layers. Since the test cooling path coupon was printed with the cooling flow direction in the vertical printing direction, the primary ridges in the roughness are aligned in the spanwise direction.

RIFT Roughness Panel Construction

The Real_x102 surface and the analog surface distributions were sectioned into four coupons 254-mm by 228.6-mm (10-in. by 9-in.) which were translated to steolithography (*.STL) files. The coupons for the roughness region for the Real_x102, Ellipsoid Analogy, and Elliptical Cone Analogy surfaces are shown in (a-c), respectively. As depicted in , 12.7-mm (0.5-in.) flat sections are added to either side of the rough surfaces in the spanwise region. These flat sections are created at the mean of the roughness of each surface and are used as structural connection which butts against the bottom faces of the RIFT sidewalls.

Summary of Geometries and Flow Conditions

Seven configurations in the RIFT and one configuration in the engine-scale test rig are considered in the present work, for a total of eight configurations. The RIFT geometric cases are, in summary: 1) the tunnel test section with smooth walls; 2-4) The Real_x102, Ellipsoid Analog, and Elliptical Cone Analog surfaces applied only to the tunnel floor; 5-7) the Real_x102, Ellipsoid Analog, and Elliptical Cone Analog surfaces applied to both the floor and ceiling of the tunnel.

The single-sided roughness tests (2-4) are similar to many previous experimental approaches including Schlichting's historical efforts. However, single-sided roughness tests in internal flows present difficulties in capturing the rough wall contributions to the total friction factor and to interpreting the appropriate hydraulic Reynolds number needed for comparison with experiments where roughness is present on all wetted surfaces. The "double-sided" roughness cases (5-8) allow more appropriate comparisons to experiments with roughness on all wetted surfaces. The double-sided tests exhibit roughness on 86.3% of the smooth-channel wetted perimeter.

Four important geometric differences exist between the RIFT double-sided cases and the L-2x-Ha channel: the RIFT has a larger aspect ratio; only the upskin face of the L-2x-Ha internal geometry is modeled in the RIFT; the RIFT cases have smooth side-walls; geometric imperfections that are not "roughness" (such as path-wandering and cross-sectional area contraction) are removed from the RIFT cases.

Each surface exhibited different lower limits of Re_{Dh} based on the low-speed surge limit of the centrifugal fan, as well as different upper limits of Re_{Dh} based on the fan and motor performance limitations. The overall Reynolds number range for the smooth-wall and rough-wall measurements is $2,000 < Re_{Dh} < 60,000$ and $20,000 < Re_{Dh} < 60,000$, respectively.

In addition to the bulk friction factor measurements, velocity profiles were acquired using hot-film anemometry. For the single-sided roughness cases, the velocity profiles were acquired at nominal Re_{Dh} values of 2×10^5 , 3×10^5 , 4×10^5 , 5×10^5 , and 6×10^5 . For the double-sided roughness cases, the velocity

profiles were acquired at nominal Re_{Dh} values of 1×10^5 , 2×10^5 , 3×10^5 , 4×10^5 , and 5×10^5 .

L-2x-Ha Flow Coupon Tests

Testing of the L-2x-Ha flow coupon was completed using the engine-scale test rig used by Stimpson and others [1] [6] [14] [15] [4]. Compressed air was fed to the coupon at a constant pressure of approximately 7 bar. Static pressure taps measured the pressure upstream and downstream of the coupon. This difference in pressure was then corrected for inlet and exit losses to the coupon, resulting in the pressure drop across the internal channels. The mass flow rate was measured using a mass flow controller. Stimpson *et al.* [1] provides a thorough analysis of the uncertainty in the measured friction factor using the present test rig. The total uncertainty is less than 8% for all L-2x-Ha friction-factor measurements with $Re_{Dh} > 4,000$. Further details on the test rig used for the flow coupons can be found in Stimpson *et al.* [1].

Roughness Internal Flow Tunnel

The Roughness Internal Flow Tunnel (RIFT) was used for the experimental measurements of friction factors and mean velocity profiles of flows interacting with surfaces exhibiting additively-manufactured roughness. The test section of the RIFT was created to have a 228.6 mm by 35.56 mm (9 in. by 1.42 in.) cross-sectional area with a roughness section length of 914 mm (36 in.). The aspect ratio of the test section is 6.3:1, and the resulting hydraulic diameter of the test section is 62.3 mm (2.45 in.). A detailed side view of the RIFT with relevant stream-wise dimensions is presented in Figure 4. The RIFT has a 254 mm (10 in.) inlet contraction with a 5:1 area ratio. Downstream of the inlet contraction, two 203-mm (8-in.) sections create an entrance length or settling region. At the beginning of the test section, a 100-mm (3.94-in.) smooth region exists created by the wind tunnel header. The total entrance length before the roughness region is 0.506 m (19.94 in.). Ceiling and floor panels that are attached to the smooth sidewalls of the tunnel define the roughness test section.

Flow through the tunnel is developed using a Fantech FX 8 XL centrifugal fan controlled using a variable autotransformer. The tunnel volumetric flow rate and average velocity are determined using a pressure tap installed in the first settling section located 58.4 mm (2 in.) downstream of the contraction exit. Based on the contraction exit static pressure, measured using an Omega, PX2650 pressure transducer with a 0-2 in.-of-water range, the volumetric flow rate is determined using Eq. (7).

$$Q = C_o A_{ts} \sqrt{\frac{2\Delta P_v}{\rho_{air}}} \quad (7)$$

where A_{ts} is the area of the test section, ΔP_v is the gage pressure measured at the contraction exit, and C_o is the discharge coefficient. The value of the discharge coefficient was determined to be 0.915 by comparison to Pitot-static

measurements acquired at the test section exit and by integrating hot-film probe velocity profiles in the test section.

The atmospheric conditions of air entering are measured using an Omega PX409-26BUSBH barometer and an Omega RH-USB relative humidity and temperature sensor. Based on the measured atmospheric conditions, the aggregate moist air density and molecular viscosity were determined using the Water and Steam saturated vapor expressions [16], Sutherland's Law [17], and Wilke's equation for gas mixtures [18].

To generate velocity profiles, the hot-film probe was installed at a location 0.902-m (35.5-in.) downstream of the start of the roughness section. The positioning system was then used to move the probe 29.2 mm (1.15 in.) vertically in increments of 0.254 mm (0.01 in.). At each y-station, four seconds of hot-film voltages were acquired at a rate of 50,000 samples per second. A fourth-order polynomial calibration curve was then used to compute the instantaneous velocity corresponding to the hot-film probe voltages. The standard error of the estimate (*SEE*) for the

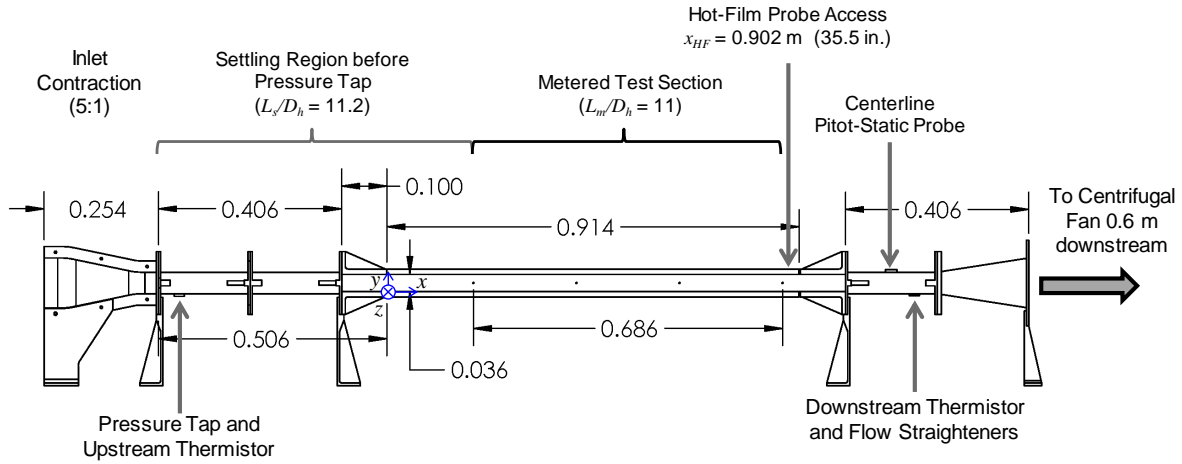


Figure 4 – Side view of RIFT (dimensions shown in meters)

Pressure taps are on each sidewall of the test section at the mid-channel height. The first (upstream) set of pressure taps is 190.5 mm (7.5 in.) downstream of the start of the roughness section. Three more sets of pressure taps were placed on the sidewalls at 228.6-mm (9-in.) intervals for a total pressure-drop metered section of 685.8 mm (27.0 in.). The Darcy-Weisbach friction factors were determined using the modified-Bernoulli major loss expression of Eq. (8):

$$\Delta P_{ts} = \frac{f_{DW} L_{ts} \rho_{air} U_{mean}^2}{D_h} = \frac{f_{DW} L_{ts} \rho_{air} Q^2}{D_h 2A_{ts}^2}. \quad (8)$$

This may be expressed entirely in terms of measured quantities:

$$f_{DW} = \frac{D_h \Delta P_{ts}}{C_0^2 L_{ts} \Delta P_v}. \quad (9)$$

In Eq. (9), ΔP_{ts} is the pressure drop between the first and last sets of pressure taps.

The velocity profile measurements were performed using a Model 1216-20 hot-film, boundary layer probe. The hot-film probe was powered using an AN-1002 constant temperature anemometer system. The hot-film probe is positioned using a single-axis, X-slide system. The positioning system includes a 1-mm/revolution ball-screw and a 400-step/revolution stepper motor, resulting in a positioning resolution of 0.0025 mm (0.0001 in.).

calibration curve to the probe calibration points was calculated to be 0.05 m/s.

Uncertainty Analysis

The uncertainties of the reduced results of volumetric flow rate, friction factor, and the Reynolds number, as defined in Eq. (10), were calculated using a Moffat [19] or perturbation-style approach.

$$Re_{D_h} = \frac{\rho_{air} D_h Q}{\mu_{air} A_{ts}} \quad (10)$$

The Moffat approach was chosen over Kline and McClintock [20] style approaches because of easier accounting of the embedded dependencies on the atmospheric temperature and relative humidity that propagate through the density and viscosity functions. Table 2 presents the measured variables and their systematic and random uncertainties. The error for the RIFT friction-factor measurements is less than one percent for all cases with $Re_{D_h} > 6,000$.

Table 2 – Direct measurement uncertainties

Meas.	Device	<i>B</i>	<i>R</i>
<i>H</i>	Calipers	2.54×10^{-5} m	-
<i>W</i>	Calipers	2.54×10^{-5} m	-
<i>L_{ts}</i>	Vertical mill gage	2.54×10^{-5} m	-
<i>T_{amb}</i>	RH-USB	1 °C	-
ϕ_{amb}	RH-USB	3%	-
<i>P_{atm}</i>	PX409-26BUSBH	16 Pa	-

ΔP_v	PX2650-2D5V	5 Pa	$\frac{tS_{\Delta P_v}}{\sqrt{N}}$
ΔP_{ts}	PX2650-0.5D5V	1.25 Pa	$\frac{tS_{\Delta P_{ts}}}{\sqrt{N}}$
u	1216-20 probe/AN-1002 CTA	0.05 m/s	$\frac{tS_u}{\sqrt{N}}$

SIMULATION METHODOLOGY

All RANS CFD simulations for the present work are generated using an in-house parallelized, cell-centered, incompressible finite-volume CFD code that accepts block-structured overset grids. Inviscid and viscous fluxes are 3rd and 2nd order accurate respectively. The Spalart-Allmaras model [21] is used for turbulence closure. All simulations for the present work are steady-state. The bulk Mach number is less than 0.05 in all of the Reynolds numbers considered for the up-scaled tunnel experiments; this is taken as justification for ignoring compressibility in the present simulations.

The test-section flow domain is discretized using a block-structured grid with approximately 53 million cells. A detail view of the surface mesh on the Real_x102 rough wall is shown in Figure 5(a). The high cell count is necessary in order to resolve the roughness geometry; grid-stretching in the stream-wise direction is inappropriate due to the highly three-dimensional nature of the roughness elements being resolved. The smooth side-walls and ceiling of the wind tunnel test section are resolved such that the first grid point is one thousandth of an inch from the wall. The rough walls have wall-spacing an order of magnitude smaller at 0.1 thousandths of an inch; this is required due to local flow acceleration that occurs over the roughness peaks. The wall-spacing used is sufficient for $y^+ < 1$ over the entire solid surface at the highest Reynolds number considered. The grid is stretched in the direction away from the solid surfaces with a growth rate of 1.1.

The wind-tunnel floor (and ceiling for the double-sided cases) one-half inch up- and down-stream of the roughness coupon is faired in the CFD simulations where the rough surface and smooth tunnel walls meet. This is done to allow use of a block-structured computational grid with no overset boundaries.

In order to maintain a manageable cell count, the 19-inch entrance length from the end of the inlet contraction to the upstream edge of the test coupon is simulated separately for each Reynolds number. The outlet velocity and turbulence profiles from this entrance-length simulation are used as inlet conditions to the roughness test section simulation. Results are re-used for all test coupon simulations. The entrance-region mesh contains approximately 3.2 million cells. The near-wall spacing is sufficient for $y^+ < 1$ for the Reynolds number range under consideration. The stream-wise spacing at the inlet to the entrance region simulation is also one thousandth of an inch. The maximum stream-wise and spanwise spacing is 0.3 inch and 0.2 inch, respectively. The inlet boundary condition is constant velocity and constant turbulence intensity ($\tilde{v}/v = 14.3$).

The channel friction factor is evaluated for the CFD in a manner analogous to the experimental measurements. The total

stream-wise force acting on the channel walls is integrated over the same length as the pressure drop measurement. The friction factor is evaluated as $f_{DW} = 8 \times F_x / \rho U_{mean}^2 A$, where F_x is the total stream-wise aerodynamic force acting on the tunnel surface within the integration area. The relevant projected surface area is $A = 2 \times (b * l + h * l)$; b is the channel width (229 mm, 9 inches), h is the channel height (36 mm, 1.42 inches), and l is 689 mm (27 inches).

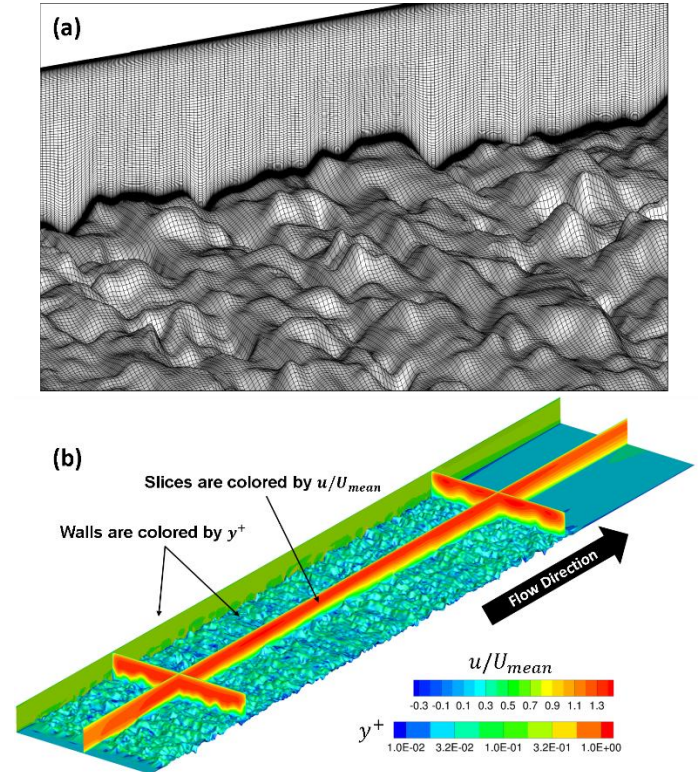


Figure 5 – (a) Detail view of the surface mesh for the single-sided Real_x102 geometry. (b) Typical CFD flow solution in the single-sided Real_x102 channel

RESULTS AND DISCUSSION

Bulk Test-Section Friction-Factor

A typical CFD flow solution for the single-sided Real_x102 channel is shown in Figure 5(b). The experimentally measured friction factors for the various channel geometries are shown in Figure 6. This figure also shows the Haaland function [22] for a smooth surface. Uncertainty bars for the RIFT measurements are smaller than the symbols in Figure 6 for $Re_{Dh} > 6,000$ and are thus omitted to reduce clutter. Error bars are also omitted for the L-2x-Ha measurements. CFD uncertainty bars (as quantified below) are shown only at the highest Reynolds number.

Above $Re_{Dh} \approx 20,000$, the measured friction factor for the smooth tunnel follows the smooth Haaland correlation to within the experimental uncertainty. Low-Reynolds number and laminar-flow effects impact the smooth-wall cases at smaller Reynolds numbers.

The L-2x-Ha friction factor falls between the measured values for the double-sided Real_x102 case and the double-sided analog surface cases. The double-sided cases were run in order to provide the most similar flow conditions in the RIFT to the conditions inside the L-2x-Ha channel in the engine-scale test rig. This provides evidence that the present approach shows promise for studying the dynamics of flow through engine-scale rough channels. Note that even though the double-sided cases are intended to be the most comparable to the L-2x-Ha case, the geometric differences between the engine-scale L-2x-Ha experiments and the scaled-up experiments make direct comparison of the measured friction-factors difficult.

The two groups of RIFT cases show the same trend in the measured friction factor. The Real_x102 (single- and double-sided) surface produces a friction factor that is ~30% higher than the corresponding analog surface cases. As is mentioned in the Analog Surface Generation section, the Real_x102 surface has large-scale span-wise ridges that the procedure for analog surface generation is unable to reproduce. These features on the Real_x102 surface introduce a degree of two-dimensionality to the bulk flow, whereas the analogy surfaces allow more 3D relief.

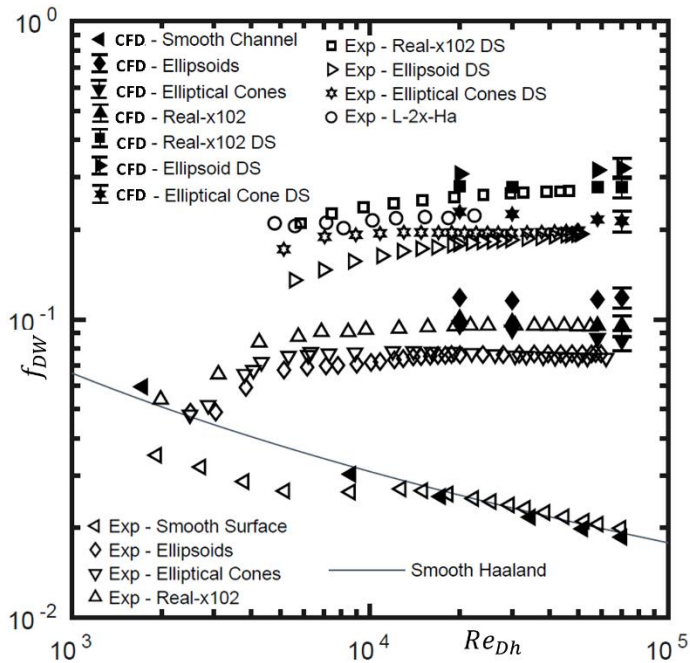


Figure 6 – Summary of friction factor measurements and CFD predictions

The Colebrook-White equation [23] (shown in Equation 11), though implicit in the friction factor, may be solved explicitly for the equivalent sand-grain roughness height as a function of the Reynolds number and friction factor. The results of doing so are shown in Table 3. This comparison shows that the Stimpson sand-grain height correlation fits the present data more closely than does the Flack-Schultz correlation.

$$\frac{1}{\sqrt{f}} = -2 \log_{10} \left(\frac{\epsilon/D_h}{3.7} + \frac{2.51}{Re \sqrt{f}} \right) \quad (11)$$

Stimpson *et al.* [13] compared measured equivalent sand-grain heights with various geometric sand-grain height correlations from the literature and found that there was significant disagreement with the measured trends. The authors hypothesized that the character of the internal flow that occurs in rough cooling channels is fundamentally different from the external flows on which the established correlations are based. The present data shows a similar trend. The Stimpson correlation is seen to predict the sand-grain heights of the present cases with reasonable success. The authors readily admit that this is not surprising, since this correlation was tuned for very similar channel flow geometries.

The Flack-Schultz correlation returns equivalent sand-grain heights that are much smaller than the results of the Stimpson correlation. The authors hypothesize that this occurs because Eq. (4) is tuned using an experimental database of flows that differ fundamentally from the internal channel flows considered here. Of the six experimental databases on which the correlation is based, four involve external flows over flat plates; the two that involve internal flow through pipes have ratios of sand-grain roughness height to hydraulic diameter four orders of magnitude smaller than in the present work. While the Flack-Schultz correlation does not capture the correct equivalent sand grain roughness values, Figure 6 and Table 3 indicate that it captures the frictional equivalence of the two analog surfaces. That is, as the Re_{Dh} values approach the region of complete turbulence the friction factors for the analog surfaces converge, when comparing either the single- or double-sided cases.

Table 3 – Equivalent sand-grain roughness height computed from the friction factor at the highest Reynolds number of each double-sided run case

	Real_x102 DS	Ellipsoid Analog DS	Elliptical Cone Analog DS
$k_{s,F-S}$ (mm)	6.933	7.045	6.965
$k_{s,St}$ (mm)	30.85	34.24	18.73
$k_{s,measured}$ (mm)	25.06	16.80	17.37
$k_{s,OVER-REL}$ (mm)	25.93	30.28	20.79
$k_{s,F-S}/D_h$	0.111	0.113	0.112
$k_{s,St}/D_h$	0.495	0.549	0.301
$k_{s,measured}/D_h$	0.402	0.269	0.279
$k_{s,OVER-REL}/D_h$	0.416	0.486	0.334

For the Real_x102 double-sided surface, the experimentally-measured equivalent sand-grain heights given in Table 3 for the double-sided Real_x102 surface yield $k_s^+ \approx 1,300$ at $Re_{Dh} = 20,000$ and $k_s^+ \approx 3,400$ at $Re_{Dh} = 47,000$. These flows are therefore in the fully rough regime at the Reynolds numbers under consideration. In this regime, form drag on the roughness elements dominates relative to viscous drag and the friction factor is approximately independent of the channel Reynolds number.

The differences between the measured and predicted friction factor for the smooth-walled, Real_x102, and Real_x102 DS cases are within the grid-uncertainty for these CFD predictions. The differences for the Elliptical Cone single- and double-sided cases are between 10% and 20%; this is slightly outside the grid-uncertainty. By contrast, the CFD predictions for the single- and double-sided Ellipsoid surface are approximately 50% above the measurements.

The authors hypothesize that the discrepancy between the measured and predicted behavior of the Ellipsoid analog surface is due to the separation and recirculation regions downstream of the individual roughness elements being poorly handled by the RANS turbulence model. The roughness elements on the Ellipsoid analog surface meet the flat substrate at almost right angles; the slope of the other two surfaces is everywhere much milder. Such aggressive backward-facing steps remain especially challenging for RANS turbulence models. More sophisticated scale-resolving approaches may provide more satisfactory agreement with experiment in future efforts.

Velocity Profiles

Velocity profiles from the floor to the ceiling of the tunnel are shown in Figure 7 in inner scaling for the smooth-walled and (single- and double-) sided Real_x102 cases for a moderate- and high- Reynolds-number case. Experimental measurements are shown as symbols and the CFD predictions are shown as solid curves. The velocity profile is located 0.902-m (35.5 inches) downstream from the leading edge of the roughness halfway between the two smooth side-walls. The friction velocity used for this plot is derived from the friction factor for the entire tunnel, not just the rough wall. That is, $u_* = \sqrt{\tau_w/\rho}$, where the apparent wall shear includes contributions from viscous and form drag for all surfaces within the test length: $\tau_w = f_{DW} \times \rho U_{mean}^2/8$. The canonical law-of-the-wall is also shown in the figure for reference.

For the (single and double-sided) Real_x102 case, a dramatic downward shift in the log-layer is observed for both the hot-film measurements and the CFD predictions. This is consistent with the expected behavior. The dominant effect of surface roughness on the boundary layer is to shift the log-layer downward when expressed in inner scaling; this was observed in the classic works of, for example, Hama [24] or Clauser [25]. CFD predictions and the hot-film measurements show broad agreement in this scaling.

CFD Grid-Refinement Study

Grid-convergence studies were performed for the smooth-wall case and for the single-sided Real_x102 case. Both studies use three grid levels and evaluate the channel friction factor at $Re_{Dh} = 20,000$. The medium grid corresponds to the level of refinement used for the other simulations in this study. A 2.54 mm (1 inch) span-wise slice was extracted from near the center of the relevant grids. The sides of the simulations were treated as symmetry planes. The number of grid points in each direction and the wall spacing was multiplied and divided by 2, respectively, to generate the fine and coarse grids. The coarse,

medium, and fine grids have 560,000, 4,440,000, and 36,740,000 cells, respectively.

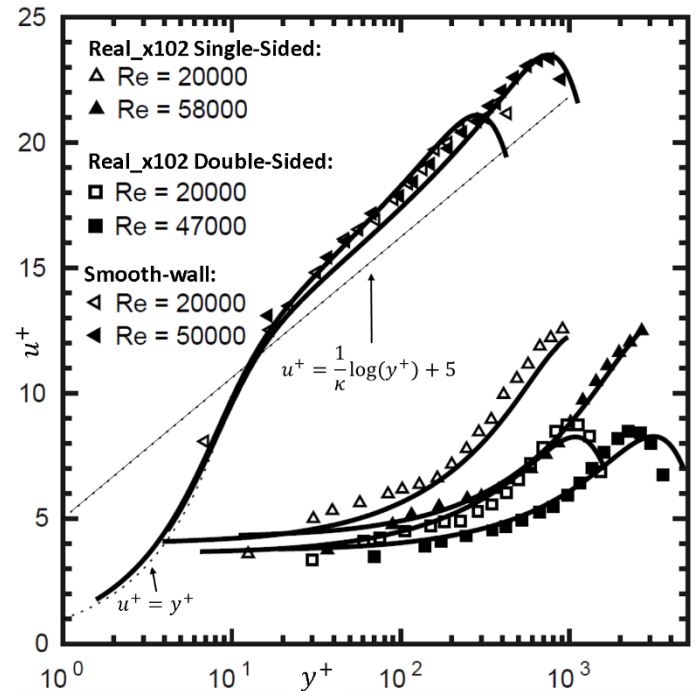


Figure 7 – Velocity profiles for the smooth-walled and single- and double-sided Real_x102 flow cases over a range of Reynolds numbers expressed in inner variables. Symbols: measurements. Curves: CFD

Table 4 shows friction-factor results for the smooth-wall and single-sided Real_x102 grid-refinement studies. The grid-convergence behavior for the smooth-wall case is as expected. Predicted friction-factors differ by less than 1% between coarse and medium meshes, and less than 0.1% between medium and fine meshes.

Table 4 – Friction-factor as a function of grid refinement for the single-sided Real_x102 surface case

	Coarse	Medium	Fine
Smooth	0.02568	0.02553	0.02546
Real_x102 single-sided	0.1495	0.1190	0.1169

Grid convergence behavior for the rough surface is somewhat different in that predicted friction-factors differ by approximately 20% between coarse and medium meshes, and 1.8% between medium and fine meshes. This suggests that the Coarse-grid may not be within the asymptotic convergence regime. As a conservative estimate, uncertainty bars of $\pm 8\%$ are shown with the CFD predictions for the friction factor of the rough surfaces at the highest Reynolds number for each case in Figure 6.

CONCLUSIONS

The present method of using up-scaled surfaces that represent roughness due to L-PBF manufacture of gas-turbine engine-scale cooling holes shows promise for future study of the fluid-dynamics problem that this roughness creates. A much fuller understanding of the turbulent flow-field is possible because of the relative ease of performing detailed flow measurements.

A gas-turbine engine-scale AM cooling channel was fabricated via L-PBF. The flow-pressure loss through the fabricated channel was measured in the engine-scale test rig over a range of Reynolds numbers. This pressure loss data provides comparison between the dynamics of flow through small, engine-scale rough channels and flow through the up-scaled rough channels tested in the RIFT. A smaller, sacrificial channel was fabricated using the same build parameters. The upskin face was selected for geometry characterization using an x-ray CT scan. The scan of the upskin face was used as the basis for all of the work that followed.

The self-organizing-map (2D-SOM-ZR) approach of McClain [8] was used to isolate the roughness from the other, non-roughness geometric imperfections from the CT scan of the upskin internal channel face. This method removed long-wavelength variations in the surface height, yielding a surrogate surface that represents the nature of the roughness created by the additive manufacturing process. The rough-surface coupon was up-scaled by a factor of 101.6 for 3D printing. The 3D-printed surface, called the Real_x102 surface, was copied and reflected in order to cover the entire floor (and ceiling) of the RIFT test section. In addition, two analog surfaces using scaled random distributions of deterministic roughness elements, produced by the procedure developed by Clemenson [9], were generated, printed, and fitted to the RIFT test section.

Pressure-loss and velocity profile measurements were performed in the RIFT for seven cases over a range of Reynolds numbers. The double-sided cases produce friction factors that straddle the friction-factor measurements at engine-scale. The double-sided Real_x102 surface produces a friction factor roughly 15% higher than the engine-scale part; the analog surfaces produce friction-factors roughly 15% lower. This correspondence between the engine-scale and tunnel-scale surfaces is promising because the goal of this work is to use up-scaled roughness models to study the flow dynamics in blade-scale cooling passages.

For both the single- and double-sided RIFT cases, the measured Real_x102 surface produced friction-factors roughly 30% higher than the analog surfaces. The authors explain this difference by noting the spanwise ridges visible on the Real_x102 surface. These ridges are not accounted for in the present method of analog surface generation. Future iterations of the method specific to engine cooling channels may include this phenomenon. The absence of spanwise ridges in the analog surface introduces 3D relief that results in a reduced friction factor.

Equivalent sand-grain roughness heights for the RIFT cases compare much more adequately with the correlation of Stimpson

than that of Flack and Schultz. This is unsurprising, since the present roughness is much larger than in the experimental databases on which the Flack-Schultz correlation is based. Also, the Stimpson correlation is tuned to match flow geometries very similar to the ones considered in this work.

While the RIFT cases compare more adequately with the correlation of Stimpson for measured equivalent sand-grain roughness, the analog surface generation approach based on the Flack and Schultz parameter match each other within 4%. That is, the Flack and Schultz parameter predicts the frictional equivalence of the two analog surfaces even though the basic statistics of the two surfaces and the basic deterministic roughness element shapes are very different.

Finally, RANS-based CFD simulations of the RIFT cases were run. Friction factor predictions for the smooth-walled and Real_x102 surface cases broadly match the experimental measurements. The comparison for the Elliptical Cone analog surfaces cases is within fifteen percent. The Ellipsoid analog surface presents more difficulty for the simulations, with predicted friction factors exceeding the measurements by approximately 50%. The authors hypothesize that this is due to the Ellipsoid analog surfaces having roughness elements that meet the substrate at nearly 90 degrees; this geometry is challenging for meshing and, in general, for RANS turbulence models.

NOMENCLATURE

A_{ts}	=	test section cross-sectional area = 8,200 mm ²
D_h	=	the RIFT hydraulic diameter = 62.3 mm (2.45 in.)
ϵ	=	the roughness element eccentricity
f_{DW}	=	Darcy-Weisbach friction factor
k_s	=	the equivalent sand-grain roughness height
L_{ts}	=	length of the RIFT pressure-drop metered section = 685.8 mm (27.0 in.)
Nm	=	roughness height relative to the 2D-SOM-ZR plane
ΔP_v	=	gage pressure at the contraction-section exit
ΔP_{ts}	=	pressure drop from first to last pressure taps
ϕ_{amb}	=	ambient relative humidity
P_{atm}	=	atmospheric pressure
Q	=	volumetric flow rate
R_a	=	the arithmetic mean roughness height
Re_{Dh}	=	Reynolds number based on the hydraulic diameter, $Re_{Dh} = \rho U_{mean} D_h / \mu$
R_q	=	the root-mean-square roughness height
Skw	=	roughness height relative skewness distribution
T_{amb}	=	ambient temperature
U_{mean}	=	average flow speed over the tunnel cross-section
u^+	=	flow velocity in wall units, $u^+ = u/u_*$
y^+	=	distance from the wall in wall units, $y^+ = \rho u_* y / \mu$

ACKNOWLEDGMENTS

This material is based upon work supported by the Department of Energy under Award Number(s) DE-FE0031280.

Disclaimer: This report was prepared as an account of work sponsored by an agency of the United States

Government. Neither the United States Government nor any agency thereof, nor any of their employees, makes any warranty, express or implied, or assumes any legal liability or responsibility for the accuracy, completeness, or usefulness of any information, apparatus, product, or process disclosed, or represents that its use would not infringe privately owned rights. Reference herein to any specific commercial product, process, or service by trade name, trademark, manufacturer, or otherwise does not necessarily constitute or imply its endorsement, recommendation, or favoring by the United States Government or any agency thereof. The views and opinions of authors expressed herein do not necessarily state or reflect those of the United States Government or any agency thereof.

BIBLIOGRAPHY

- [1] C. Stimpson, J. Snyder, K. Thole and D. Mongillo, "Roughness Effects on Flow and Heat Transfer for Additively Manufactured Channels," *J. TURBOMACH*, 2016.
- [2] C. Stimpson, J. Snyder, K. Thole and D. Mongillo, "Scaling Roughness Effects on Pressure Loss and Heat Transfer of Additively Manufactured Channel," *J. TURBOMACH*, vol. 139, 2017.
- [3] K. Flack and M. Schultz, "Review of Hydraulic Roughness Scales in the Fully Rough Regime," *Journal of Fluids Engineering*, vol. 132, 2010.
- [4] J. Snyder, C. Stimpson, K. Thole and D. Mongillo, "Build Direction Effects on Additively Manufactured Channel," *J. TURBOMACH*, vol. 138, no. 5, 2016.
- [5] K. Kirsch and K. Thole, "Heat Transfer and Pressure Loss Measurements in Additively Manufactured Wavy Microchannel," *J. TURBOMACH*, vol. 139, 2017.
- [6] K. Kirsch and K. Thole, "Experimental Investigation of Numerically Optimized Wavy Microchannels Created Through Additive Manufacturing," in *Proceedings of the ASME Turbo Expo 2017: Turbomachinery Technical Conference and Exposition*, Charlotte, NC, 2017.
- [7] K. Kirsch and K. Thole, "Isolating the Effects of Surface Roughness Versus Wall Shape in Numerically Optimized, Additively Manufactured Micro Cooling Channels," *Experimental Thermal and Fluid Science*, vol. 98, 2018.
- [8] S. McClain, "Spanwise Form Extraction for Ice Roughness Measurements from Misaligned Airfoils or Tapered Wings," in *9th AIAA Atmospheric and Space Environments Conference*, Denver, CO, 2017.
- [9] J.-M. Clemenson, T. Shannon and S. McClain, "A Novel Method for Constructing Analog Roughness Patterns to Replicate Ice Accretion Characteristics," in *2018 Atmospheric and Space Environments Conference*, Atlanta, Georgia, 2018.
- [10] *Material DataSheet: EOS Nickel Alloy HX*, 2014.
- [11] B. Becker, D. Maier and C. Reinhart, "Computer Tomography Has Arrived in Automated Inspection Processes," in *Proceedings of the 18th World Conference on Non-Destructive Testing*, 2012.
- [12] L. Tecson and S. McClain, "Modeling of Realistic Ice Roughness Element Distributions to Characterize Convective Heat Transfer," in *5th AIAA Atmospheric and Space Environments Conference*, San Diego, CA, 2013.
- [13] C. Stimpson, J. Snyder, K. Thole and D. Mongillo, "Scaling Roughness Effects on Pressure Loss and Heat Transfer in Additively Manufactured Channels," *J. TURBOMACH*, vol. 139, 2017.
- [14] K. Kirsch and K. Thole, "Pressure Loss and Heat Transfer Performance of Additively and Conventionally Manufactured Pin Fin Arrays," *International Journal of Heat and Mass Transfer*, vol. 108, 2017.
- [15] K. Ferster, K. Kirsch and K. Thole, "Effects of Geometry, Spacing, and Number of Pin Fins in Additively Manufactured Microchannel Pin Fin Arrays," *J. TURBOMACH*, vol. 140, no. 1, 2017.
- [16] The International Association for the Properties of Water and Steam, "Revised Release on the IAPWS Industrial Formulation 1997 for the Thermodynamic Properties of Water and Steam," 2007. [Online]. Available: <http://www.iapws.org>.
- [17] W. Sutherland, "The Viscosity of Gases and Molecular Force," *Philos. Mag.*, vol. 5, 1983.
- [18] C. Wilke, "A Viscosity Equation for Gas Mixtures," *Journal of Chemical Physics*, vol. 18, no. 4, 1950.
- [19] R. Moffat, "Describing Uncertainties in Experimental Results," *Experimental Thermal and Fluid Sciences*, 1988.
- [20] S. Kline and F. McClintock, "Describing Uncertainties in Single Sample Experiments," *Mechanical Engineering*, 1953.
- [21] P. Spalart and S. Allmaras, "A One-Equation Turbulence Model for Aerodynamic Flows," in *30th Aerospace Sciences Meeting and Exhibit*, Reston, Virginia, 1992.
- [22] S. Haaland, "Simple and Explicit Formulas for the Friction Factor in Turbulent Pipe Flow," *Journal of Fluids Engineering*, vol. 105, 1983.
- [23] C. Colebrook, "Turbulent Flow in Pipes, with Particular Reference to the Transition Region between the Smooth and Rough Pipe Laws," *Journal of the Institution of Civil Engineers*, vol. 11, no. 4, 1939.
- [24] F. Hama, "Boundary-Layer Characteristics for Smooth and Rough Surfaces," *Transactions of the Society of Naval Architecture*, vol. 62, 1954.
- [25] F. Clauser, "The Turbulent Boundary Layer," *Advances in Applied Mechanics*, vol. 4, 1956.